Available online at www.sciencedirect.com
ScienceDirect
Nuclear Physics B Proceedings Supplement 00 (2014) 1–6
Nuclear Physics B Proceedings Supplement

Simultaneous measurements of the $t\bar{t}$, W^+W^-, and $Z/\gamma^* \to \tau\tau$ production cross-sections in pp collisions at $\sqrt{s} = 7$ TeV with the ATLAS detector☆

Antonio Limosani† on behalf of the ATLAS collaboration

†*University of Sydney, Australia*

Abstract

Simultaneous measurements of the $t\bar{t}$, W^+W^-, and $Z/\gamma^* \to \tau\tau$ production cross-sections using an integrated luminosity of 4.6 fb^{-1} of pp collisions at $\sqrt{s} = 7$ TeV collected by the ATLAS detector at the LHC are presented. Events are selected with two high transverse momentum leptons consisting of an oppositely charged electron and muon pair. The three processes are separated using the distributions of the missing transverse momentum of events with zero and greater than zero jet multiplicities. Measurements of the fiducial cross-section are presented along with results that quantify for the first time the underlying correlations in the predicted and measured cross-sections due to proton parton distribution functions. These results indicate that the correlated NLO predictions for $t\bar{t}$ and $Z/\gamma^* \to \tau\tau$ significantly underestimate the data, while those at NNLO generally describe the data well. The full cross-sections are measured to be $\sigma(t\bar{t}) = 181.2 \pm 2.8^{+9.7}_{-9.5} \pm 3.3 \pm 3.3$ pb, $\sigma(W^+W^-) = 53.3 \pm 2.7^{+7.3}_{-8.0} \pm 1.0 \pm 0.5$ pb, and $\sigma(Z/\gamma^* \to \tau\tau) = 1174 \pm 24^{+72}_{-87} \pm 21 \pm 9$ pb, where the cited uncertainties are due to statistics, systematic effects, luminosity and the LHC beam energy measurement, respectively.

Keywords:

1. Introduction

Proton collisions at the LHC have large cross-sections for the production of top quark pairs, W boson pairs, and Z bosons. The cross-section for each of these processes is predicted to a high precision within the standard model (SM) of particle physics. In this article, a global test of these SM predictions is presented through the study of the common final state including an oppositely charged electron and muon pair ($e\mu$ events). Specifically, a simultaneous measurement of the cross-sections of the pair production of top quarks ($t\bar{t}$), W bosons (W^+W^-, written as WW), and tau-leptons via the Drell–Yan mechanism ($Z/\gamma^* \to \tau\tau$) is performed. These processes are considered in a two-dimensional parameter space spanned by the missing transverse momentum, $E_{\mathrm{T}}^{\mathrm{miss}}$, and jet multiplicity, N_{jets}, where they are naturally well separated, allowing the simultaneous extraction of their cross-sections. Events from $t\bar{t}$ production tend to have large $E_{\mathrm{T}}^{\mathrm{miss}}$ and large N_{jets}, whereas WW events tend to have large $E_{\mathrm{T}}^{\mathrm{miss}}$ and small N_{jets}, and $Z/\gamma^* \to \tau\tau$ events are characterized by small $E_{\mathrm{T}}^{\mathrm{miss}}$ and even smaller N_{jets}.

This analysis of $e\mu$ events allows a broader test of the SM than that given by dedicated cross-section measurements, and provides a first simultaneous measurement of the production cross-sections for the processes of interest at the LHC. This simultaneous measurement unifies the definitions of fiducial region, physics object and event selections, and estimation of uncertainties for each signal measurement. In particular these measurements offer a new window on the effects of the parton distribution function (PDF) through consideration of the correlations between pairs of production cross-sections, induced by the use of common PDF predictions. An improved understanding of these processes can improve

Email address: antonio.limosani@sydney.edu.au (Antonio Limosani† on behalf of the ATLAS collaboration)

the theoretical calculations and methods used in their study, and thereby more precisely constrain background predictions for future new physics searches at the LHC.

The measurement technique used here was first used by the CDF experiment at the Tevatron [1] using the $p\bar{p}$ collision data at a center-of-mass energy, $\sqrt{s}$, of 1.96 TeV. In this paper the results are obtained from $\sqrt{s} = 7\,\text{TeV}$ pp collision data collected by the ATLAS detector [2] at the LHC corresponding to an integrated luminosity of 4.6 fb^{-1} [3]. Previous dedicated measurements of these cross-sections in the dilepton channel were performed by ATLAS using data samples of 4.6 fb^{-1} for $t\bar{t}$ [5] and WW [6], and 36 pb^{-1} for $Z/\gamma^* \to \tau\tau$ [7]. The analysis and results presented here are examined in greater detail in Ref. [4].

2. The ATLAS detector

The ATLAS detector [2] is a multi-purpose particle physics detector with approximately forward-backward symmetric cylindrical geometry. It includes an inner detector (ID) system is immersed in a 2 T axial magnetic field and provides tracking information for charged particles in the pseudorapidity range $|\eta| < 2.5$ [1]. Calorimeter systems with either liquid argon or scintillating tiles as the active media provide energy measurements over the range $|\eta| < 4.9$. The muon detectors outside the calorimeters are contained in a toroidal magnetic field produced by air-core superconducting magnets with field integrals varying from $1\,\text{T}\cdot\text{m}$ to $8\,\text{T}\cdot\text{m}$. They provide trigger and high-precision tracking capabilities for $|\eta| < 2.4$ and $|\eta| < 2.7$, respectively.

3. Data and Monte Carlo Samples

Several Monte Carlo (MC) based generators are used to simulate SM processes for the baseline estimate of efficiency factors and for deriving the expected distributions in the 2D phase space (templates). MC events are generated at $\sqrt{s} = 7$ TeV and processed through the full detector simulation [8] based on GEANT4 [9]. The simulation includes modelling additional pp interactions in the same and neighbouring bunch crossings. The MC events are subsequently re-weighted such that the simulated instantaneous luminosity distribution matches that in data. All baseline samples use next-to-leading order (NLO) parton distribution functions (PDFs) CT10 [10] with the underlying event modelled with HERWIG [11] and JIMMY [12]. Production of top quark pairs, was performed using the NLO generator MC@NLO v4.01 [13] with a top quark mass of 172.5 GeV. Single top production, which is considered a background, is generated with MC@NLO by applying the diagram removal scheme [15, 16] of overlaps with $t\bar{t}$ final states. The single top cross-section is provided at approximate NNLO, $\sigma^{Wt}_{\text{theory}} = 15.7 \pm 1.1$ pb [19]. Baseline WW samples are simulated with MC@NLO ($q\bar{q} \to WW$), gg2WW (gluon fusion) [17], and POWHEG (Higgs Boson) [18]. The $Z/\gamma^* \to \tau\tau$ and associated jets process was simulated using SHERPA v1.4.0 [20]. Baseline samples for background diboson processes, WZ and ZZ, were simulated using ALPGEN [21], with cross-sections calculated with MCFM [22] with MSTW2008 NLO PDFs [23], and found to be $\sigma^{WZ}_{\text{NLO}} = 17.8 \pm 1.3$ pb and $\sigma^{ZZ}_{\text{NLO}} = 5.9 \pm 0.3$ pb. The TAUOLA [24] and PHOTOS [25] packages are used in the generation of all samples, except SHERPA, to model the decay of the τ leptons and QED final state-state radiation of photons respectively. Alternative samples for evaluating systematic uncertainties for: modelling include those generated using ALPGEN, POWHEG and SHERPA; hadronization include samples with variations between HERWIG and PYTHIA for parton showering; and for initial and final state radiation include samples with variations of tune parameters with ALPGEN generated samples. Corrections to the selection efficiency of leptons are applied to the MC and the simulation is tuned to reproduce the calorimeter energy and, the muon momentum scale and resolution observed in data. This improves the agreement between data and simulation.

4. Object and event selection

Electrons must satisfy tight identification criteria [26] and fulfill $|\eta| < 2.47$ with an exception of $1.37 < |\eta| < 1.52$ to exclude the transition region between barrel and endcaps of the calorimeter, and $E_T > 25$ GeV, where $|\eta|$ and E_T are determined from calibrated clustered energy deposits in the electromagnetic calorimeter matched to an ID track. Muons are reconstructed by combining tracks in the ID and tracks in the muon spectrometer [27]. Reconstructed muons are considered as candidates if they have $p_{\text{T}} > 20\,\text{GeV}$ and $|\eta| < 2.4$. Muon candidates arising from cosmic rays are rejected by removing candidate pairs that are back-to-back in the transverse plane and that have transverse impact parameter

[1] ATLAS uses a right-handed coordinate system with its origin at the nominal interaction point (IP) in the centre of the detector and the z-axis along the beam pipe. The x-axis points from the IP to the centre of the LHC ring, and the y-axis points upward. Cylindrical coordinates (R, ϕ) are used in the transverse plane, ϕ being the azimuthal angle around the beam pipe. The pseudorapidity is defined in terms of the polar angle θ as $\eta = -\ln\tan(\theta/2)$.

relative to the beam axis $|d_0| > 0.5$ mm. Events that contain an electron candidate which overlaps with a loosely reconstructed muon are vetoed.

Each lepton is required to be compatible with being produced at the primary vertex by having a longitudinal impact parameter smaller than 2 mm. To suppress the contribution from hadronic jets which are misidentified as leptons, electron and muon candidates are required to be isolated in both the ID and the calorimeter [4].

Jets are reconstructed from clustered energy deposits in the calorimeters using the anti-k_t algorithm [28] with a radius parameter $R = 0.4$. Their energies are corrected to correspond on average to the total energy of the stable particles emitted towards the jet using energy- and η-dependent correction factors derived from simulation, and a residual correction derived from in situ measurements [29, 30, 31, 32]. They are required to have $p_{\mathrm{T}} > 25$ GeV and $|\eta| < 2.5$. Furthermore, at least 75% of the scalar sum of the p_{T} of all the tracks associated with each jet must belong to tracks originating from the primary vertex, which is defined as the vertex with the highest sum of the squared p_{T} values of the associated tracks in the event. The $E_{\mathrm{T}}^{\mathrm{miss}}$ is calculated [33] as the magnitude of the negative of the vectorial sum of all energy deposits in the calorimeters, and then corrected for the momenta of the reconstructed muons.

5. Backgrounds

Backgrounds include irreducible components Wt, WZ and ZZ, which are determined from MC, using samples and cross-sections described above, and a reducible component from fake or non-prompt leptons, which may include a lepton from a heavy quark decay, fakes from jets, and an electron from an isolated photon conversion. This background is estimated using a "matrix method" similar to that described in Ref. [34]. Therefore in addition to the data signal region, which in this context is denoted the TT region (both electron and muon candidates satisfy "tight" requirements), there are three data sideband regions denoted TL, LT, and LL, where L corresponds to a candidate lepton passing loose but failing tight requirements. With respect to tight requirements loose leptons are those where isolation requirements are removed and in addition, for electrons, identification requirements are relaxed. The "matrix method" solves a set of four linear equations that depend on four inputs of real lepton (r_e and r_μ) and fake and non-prompt lepton probabilities (f_e and f_μ), which are calculated as the ratio of a candidate passing tight requirements given loose requirements are passed.

Probabilities $r_e(= 0.75 - 0.81)$ and $r_\mu(= 0.94 - 0.97)$ are measured in data dominated by $Z \to ee$ and $Z \to \mu\mu$ decays whilst $f_e(= 0.15-0.30)$ and $f_\mu(= 0.13-0.18)$ are measured in data dominated by QCD multijet events. The values vary and are subsequently parameterised according to lepton p_T, lepton η and N_{jets}. For checking the measurements of r and f, events where the W+jets processes dominate are used as control regions, which show agreement between background predictions and data within uncertainties. In addition a same-sign charge control region, which is dominated by a fake and non-prompt contribution, where the opposite charge sign requirement in this analysis is inverted, showed agreement within uncertainties in both $E_{\mathrm{T}}^{\mathrm{miss}}$ and N_{jets} distributions between data and expectation. In addition the matrix method was used to predict the background in MC events, which is found to agree within uncertainties with the estimate derived from truth information.

After object and event selection the data yields 12224 $e\mu$ events compared with an expectation of 11700 ± 600 events, which is calculated using predictions of 5900 ($t\bar{t}$), 3500 ($Z/\gamma^* \to \tau\tau$), 1400 (WW), 590 (Wt), 90 (WZ and ZZ) and 210 (fake and non-prompt).

6. Template fit method

Templates in the $E_{\mathrm{T}}^{\mathrm{miss}}$-$N_{\mathrm{jets}}$ parameter space are produced for signal processes ($t\bar{t}$, WW, $Z/\gamma^* \to \tau\tau$) and backgrounds (Wt, WZ/ZZ, non-prompt/fake $e\mu$) using the object and event selection described above, and are employed in a binned maximum likelihood fit to data. The parameter space is divided into two bins for jet multiplicity, $N_{\mathrm{jets}} = 0$ and $N_{\mathrm{jets}} \geq 1$ whilst $E_{\mathrm{T}}^{\mathrm{miss}}$ is divided into twenty bins from $0 < E_{\mathrm{T}}^{\mathrm{miss}} < 200^{+}$ GeV in increments of 10 GeV, with the last bin containing the overflow.

The likelihood in a given bin is taken as a Poisson distribution, and the negative log of the product of bin likelihoods in minimized using MINUIT [35]. The normalizations of the $t\bar{t}$, WW and $Z/\gamma^* \to \tau\tau$ templates are treated as free parameters in the fit, whereas the normalizations of the Wt and WZ/ZZ templates are constrained to their expected values from theory. Symmetrized systematic uncertainties owing to variations in $e\mu$ efficiencies, cross sections, and the luminosity are incorporated through Gaussian constraints, which are included as additive terms to the log-likelihood.

To minimize the theoretical uncertainty due to the extrapolation from the measured to the total phase space for the cross-section measurement, a fiducial phase space is defined by parton-level quantities chosen to be

similar to the selection criteria used in the fully reconstructed sample. Electron objects must have transverse energy $E_{\mathrm{T}} > 25$ GeV and pseudorapidity $|\eta| < 2.47$, excluding the transition region $1.37 < |\eta| < 1.52$. Muon objects are required to have transverse momentum $p_{\mathrm{T}} > 20$ GeV and pseudorapidity $|\eta| < 2.5$. All selected electron or muon objects must be flagged as stable final state particles in the generator record and must originate from a decay vertex associated with a W boson from the hard scattering process, or from tau lepton decays which themselves are associated to such a W or Z decay. Contributions from final state radiation at truth level in a $\Delta R = 0.1$ cone centered on the lepton candidate are added to the four-momentum of the lepton candidate. The fiducial cross-section σ_{fid} for the $pp \to X$ processes, with X producing an $e\mu$ final state, is calculated as $\sigma_{\mathrm{fid}}^{pp\to X} = \frac{N_X^{\mathrm{fid}}}{C^{pp\to X}\cdot\mathcal{L}}$, where $C^{pp\to X}$ is the ratio of the number of events fulfilling the offline selection criteria to the number of events produced in the fiducial phase space estimated from simulation and N_X^{fid} is the number of events attributed to the specified process by the fit using systematic uncertainties implemented through Gaussian constraints that affect $C^{pp\to X}$. Lastly $\mathcal{L}$ corresponds to the integrated luminosity of the data sample (4.6 fb^{-1}). By extension the total production cross-section is determined using $\sigma_{\mathrm{tot}}^{pp\to X} = \frac{N_X^{\mathrm{tot}}}{\mathcal{A}^{pp\to X}\cdot C^{pp\to X}\cdot \mathcal{B}^{X\to e\mu+Y}\cdot\mathcal{L}}$, where, similarly, N_X^{tot} is the number of events using systematic uncertainties that affect the product $\mathcal{A}^{pp\to X}C^{pp\to X}$, where $\mathcal{A}^{pp\to X}$ represents the kinematic and geometric acceptance in the fiducial phase space as a fraction of the total; and $\mathcal{B}^{X\to e\mu+Y}$ is the branching fraction to inclusive $e\mu$ final states for the decay channel under consideration.

7. Fit and cross-section results

The results of the fit to data are displayed in Fig.1, which shows the $E_{\mathrm{T}}^{\mathrm{miss}}$ distribution in each bin of jet multiplicity considered. For $N_{\mathrm{jets}}= 0$, the dominant components are $Z/\gamma^* \to \tau\tau$ and WW whilst for $N_{\mathrm{jets}}\geq 1$ $t\bar{t}$ is dominant. The hatched shading centered on the sum of the contributions in each bin shows the total uncertainty. As shown the fit is able to reconcile the signal components to the data fairly well. The yields for the signal processes returned from the fit are given in Table 1, along with the extrapolation factors and subsequent fiducial and total cross-sections with accompanying uncertainties. Within the fiducial region, uncertainties come mainly from detector or experimental sources and template shape uncertainties.

8. Systematic uncertainties

Systematics uncertainties assessed due to lepton object selection include effects of: triggering; combined effects of reconstruction, identification, isolation (eREC); scale; and resolution. Those assessed for jet object selection include the jet energy scale (JES), reconstruction, resolution and jet vertex fraction and for $E_{\mathrm{T}}^{\mathrm{miss}}$ include effects due to out of calorimeter cell contributions (CELLOUT) and pileup. For individual processes effects of initial and final state radiation (IFSR), parton showering (PS) and generator modelling are also considered. The latter set affects $\mathcal{A}C$ and C factors differently, where, in general, the uncertainty on C is less than that for $\mathcal{A}$ as expected. Uncertainties due to the fake and non-prompt background and the parton distribution function modelling and underlying parameters are not introduced as Gaussian constraints in the likelihood and not estimated using pseudo MC owing to the large number of parameters on which they depend. Rather, cross-sections are re-determined for a given variation and then the maximum positive and negative deviations from the central values are assigned as the uncertainty. PDF sets used apart from the default, CT10, include MSTW2008 and NNPDF2.3, and within each set parameters are varied. Matrix method probabilities are varied within their errors to derive alternative estimates for the fake and non-prompt background (FNP).

Uncertainties on $\mathcal{A}$ and C other than those associated to parton distribution functions are included as Gaussian constraints. Template shape uncertainties are estimated using a pseudo MC technique where 1000 ensembles of distributions of signal processes are generated according to expectation from MC and theory predictions and combined together to produce a sample pseudo data distribution (PE). Each PE is subsequently fitted with modified templates that are formed when a given source of systematic uncertainty is varied up and down by its expected uncertainty. The difference between the mean value of the N_{sig} distribution and the expected value used to generate pseudo data, ΔN_{sig}, is taken as the uncertainty due to template shape effects. To obtain the final template shape uncertainty, each positive $\Delta N_{\mathrm{sig}}/N_{\mathrm{sig}}$ value is added quadratically to obtain the total positive uncertainty, and each negative value is added likewise to obtain the negative uncertainty.

Uncertainties of significance affecting all processes include electron REC (3%), parton showering (3%), and PDFs (1.5%-1.7%). Other dominant uncertainties individually are: on $t\bar{t}$ include JES (1.4%); on $Z/\gamma^* \to \tau\tau$ include CELLOUT (2.3%), and pileup (1.7%); and on

Table 1: Summary of fitted yields, acceptance correction factors, and cross-section measurments. Column two presents the number of signal events delivered by the fit. The acceptance correction factors in columns three and four, $\mathcal{A}$ and C, are extracted from Monte Carlo samples. The branching ratios $\mathcal{B}$ in column five are taken from the best theoretical calculations or experimental measurements [36]. The fiducial and total cross-sections are shown in the final two columns, where uncertainties shown are due to statistics, systematics, the luminosity, and LHC beam energy, respectively.

Process	N_{fit}	$\mathcal{A}C$	C	$\mathcal{B}$	Fiducial σ [fb]	Total σ [fb]	Prediction σ [fb]
$t\bar{t}$	6049	0.224	0.482	0.0324	$2730 \pm 40 \pm 140 \pm 50 \pm 50$	$181.2 \pm 2.8\,^{+9.7}_{-9.5} \pm 3.3 \pm 3.3$	177 ± 11 [37]
WW	1479	0.187	0.505	0.0324	$638 \pm 32\,^{+88}_{-95} \pm 11 \pm 6$	$53.3 \pm 2.7\,^{+7.3}_{-8.0} \pm 1.0 \pm 0.5$	49.2 ± 2.3 [39]
$Z/\gamma^* \to \tau\tau$	3845	0.0115	0.496	0.0621	$1690 \pm 35\,^{+89}_{-116} \pm 30 \pm 14$	$1174 \pm 24\,^{+72}_{-87} \pm 21 \pm 9$	1070 ± 54 [23, 38]

WW include CELLOUT (10%), FNP (6%) and generator modelling (5%).

9. Discussion of results

Measurements are consistent with the latest theoretical predictions to NNLO in QCD for $t\bar{t}$ [37] and $Z/\gamma^* \to \tau\tau$ [38], and to NLO in QCD for WW [39]. In addition this method allows for a comparison with theoretical correlations between pairs of processes which arise through the assumed parton distribution functions. One of the primary motivations for performing a simultaneous measurement is to have the signal processes well separated in some phase space so that a unique global minimum of the fit function can be found—but with enough overlap between signal processes that the templates can constrain each other in these overlap regions, leading to globally consistent measurements over the whole phase space. Thus the anti-correlations resulting from these constraints, between signal event yields from the fit procedure, are shown in Figure 2 together with theoretical predictions. The WW template overlaps both the $t\bar{t}$ and $Z/\gamma^* \to \tau\tau$ templates and the WW yield is anti-correlated with both as a result. The measurements shown here demonstrate consistency with NNLO predictions as opposed to NLO taking into account correlations of the underlying parton distribution functions. These comparisons are the first of their kind and are a unique feature of this analysis.

10. Conclusion

In summary, simultaneous measurements of $t\bar{t}$, $Z/\gamma^* \to \tau\tau$ and WW in the final state of exactly one electron and one muon of opposite charge are reported. The analysis is based on 4.6 fb^{-1} of proton-proton collision data delivered by the LHC at $\sqrt{s} = 7$ TeV. Measurements are found to be within uncertainty of NNLO predictions for $t\bar{t}$ and $Z/\gamma^* \to \tau\tau$. The WW measurement includes contributions from gluon fusion production via non-resonant and resonant (Higgs boson) channels, and is found to be within uncertainty of the NLO prediction. This analysis is the first simultaneous measurement of these cross-sections with a full treatment of systematic uncertainties at $\sqrt{s} = 7$ TeV.

References

[1] A. Abulencia *et al.*,Phys. Rev. D **78**, 012003 (2008)
[2] ATLAS Collaboration, JINST **3**, S08003 (2008).
[3] ATLAS Collaboration, Eur. Phys. J. C **73**, 2518 (2013)
[4] ATLAS Collaboration, arXiv:1407.0573 [hep-ex]. Submitted to Physical Review D
[5] ATLAS Collaboration, arXiv:1406.5375 [hep-ex].
[6] ATLAS Collaboration, Phys. Rev. D **87**, no. 11, 112001 (2013) [Erratum-ibid. D **88**, no. 7, 079906 (2013)] [arXiv:1210.2979 [hep-ex]].
[7] ATLAS Collaboration, Phys. Rev. D **84**, 112006 (2011) [arXiv:1108.2016 [hep-ex]].
[8] ATLAS Collaboration, Eur. Phys. J. C **70**, 823 (2010)
[9] J. Allison, K. Amako, J. Apostolakis, H. Araujo, P. A. Dubois, M. Asai, G. Barrand and R. Capra *et al.*, IEEE Trans. Nucl. Sci. **53**, 270 (2006).
[10] H. -L. Lai, M. Guzzi, J. Huston, Z. Li, P. M. Nadolsky, J. Pumplin and C. -P. Yuan, Phys. Rev. D **82**, 074024 (2010)
[11] G. Corcella, I. G. Knowles, G. Marchesini, S. Moretti, K. Odagiri, P. Richardson, M. H. Seymour and B. R. Webber, JHEP **0101**, 010 (2001)
[12] J. M. Butterworth, J. R. Forshaw and M. H. Seymour, Z. Phys. C **72**, 637 (1996)
[13] S. Frixione and B. R. Webber, JHEP **0206**, 029 (2002)
[14] S. Frixione, E. Laenen, P. Motylinski and B. R. Webber, JHEP **0603**, 092 (2006)
[15] S. Frixione, E. Laenen, P. Motylinski, B. R. Webber and C. D. White, JHEP **0807**, 029 (2008) [arXiv:0805.3067 [hep-ph]].
[16] S. Frixione, E. Laenen, P. Motylinski, B. R. Webber and C. D. White, JHEP **0807**, 029 (2008)
[17] N. Kauer and G. Passarino, JHEP **1208**, 116 (2012) [arXiv:1206.4803 [hep-ph]].
[18] S. Alioli, P. Nason, C. Oleari and E. Re, JHEP **0904**, 002 (2009) [arXiv:0812.0578 [hep-ph]].
[19] N. Kidonakis, Phys. Rev. D **82**, 054018 (2010)
[20] T. Gleisberg, S. .Hoeche, F. Krauss, M. Schonherr, S. Schumann, F. Siegert and J. Winter, JHEP **0902**, 007 (2009)
[21] M. L. Mangano, M. Moretti, F. Piccinini, R. Pittau and A. D. Polosa, JHEP **0307**, 001 (2003)
[22] J. M. Campbell, R. K. Ellis and D. L. Rainwater, Phys. Rev. D **68**, 094021 (2003)
[23] A. D. Martin, W. J. Stirling, R. S. Thorne and G. Watt, Eur. Phys. J. C **63**, 189 (2009)
[24] S. Jadach, Z. Was, R. Decker and J. H. Kuhn, Comput. Phys. Commun. **76**, 361 (1993).

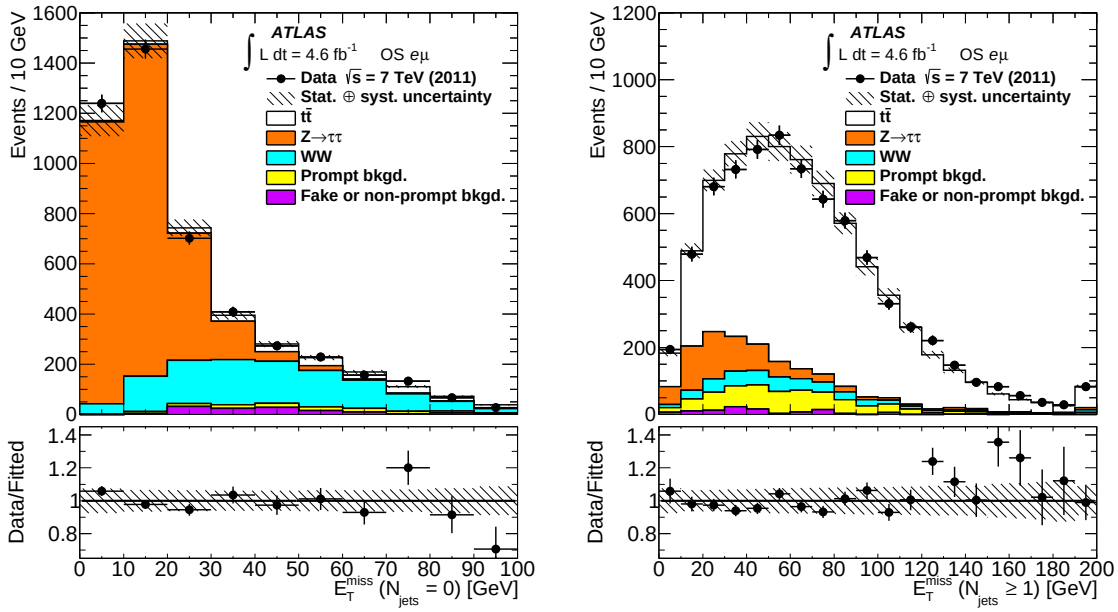

Figure 1: The result of the fit to data displaying the $E_{\mathrm{T}}^{\mathrm{miss}}$ distribution for (LEFT) $N_{\mathrm{jets}} = 0$ and (RIGHT) $N_{\mathrm{jets}} \geq 1$ for events producing exactly one electron and one muon of opposite sign charge in both data and Monte Carlo samples (including data-driven fakes estimate) [5].

[25] E. Barberio and Z. Was, Comput. Phys. Commun. **79**, 291 (1994).
[26] ATLAS Collaboration, Eur. Phys. J. C **72**, 1909 (2012)
[27] ATLAS Collaboration, Phys. Lett. B **707**, 438 (2012)
[28] M. Cacciari, G. P. Salam and G. Soyez, JHEP **0804**, 063 (2008)
[29] ATLAS Collaboration, Eur. Phys. J. C **73**, 2304 (2013) [arXiv:1112.6426 [hep-ex]].
[30] ATLAS Collaboration, JINST **9**, P07024 (2014) [arXiv:1405.3768 [hep-ex]].
[31] ATLAS Collaboration,Eur. Phys. J. C **70**, 1193 (2010) [arXiv:1007.5423 [physics.ins-det]].
[32] ATLAS Collaboration, arXiv:1406.0076 [hep-ex].
[33] ATLAS Collaboration, Eur. Phys. J. C **72**, 1844 (2012)
[34] ATLAS Collaboration, Eur. Phys. J. C **71**, 1577 (2011)
[35] F. James and M. Roos, Comput. Phys. Commun. **10**, 343 (1975).
[36] K. Nakamura *et al.*,J. Phys. G **37**, 075021 (2010).
[37] M. Czakon, P. Fiedler and A. Mitov, Phys. Rev. Lett. **110**, 252004 (2013)
[38] R. Gavin, Y. Li, F. Petriello and S. Quackenbush, Comput. Phys. Commun. **182**, 2388 (2011)
[39] J. M. Campbell, E. Castaneda-Miranda, Y. Fang, N. Kauer, B. Mellado and S. L. Wu, Phys. Rev. D **80** (2009) 054023

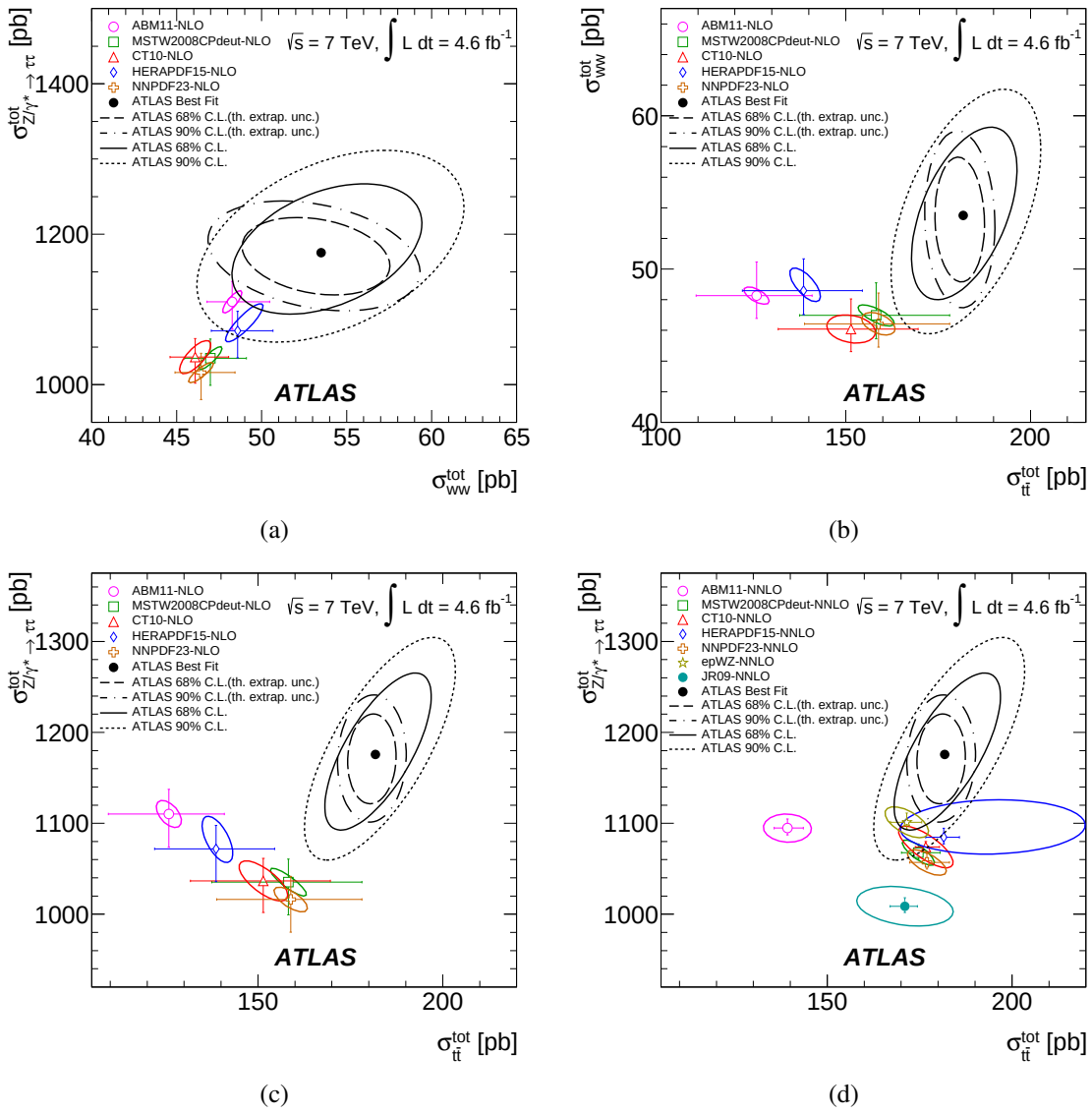

Figure 2: Contours of the profile likelihood function as a function of two production cross-sections of interest: (a) $\sigma_{Z/\gamma^* \to \tau\tau}$ and σ_{WW} at compared to NLO predictions; (b) σ_{WW} and $\sigma_{t\bar{t}}$ at NLO compared to NLO predictions; (c,d) $\sigma_{Z/\gamma^* \to \tau\tau}$ and $\sigma_{t\bar{t}}$ at compared to NLO and NNLO predictions. Contours labelled "theory uncertainty" are obtained by constructing a likelihood function with only theoretical uncertainties. The contours are fitted to ellipses and the ellipses are enlarged according to shape, fake, and PDF uncertainties (theory uncertainty ellipses are enlarged only be theoretical shape uncertainties). Theoretical cross-section predictions are shown at next-to-leading order (a,b,c) and next-to-next-to-leading order (d) for $t\bar{t}$ and $Z/\gamma^* \to \tau\tau$. Ellipses around theoretical predictions represent the correlated uncertainties due to PDFs, while error bars represent uncertainties due to choice of scale μ_F and μ_R [5].